# Design, Construction, and Analysis of a Large Scale Inner Stator Radial Flux Magnetically Geared Generator for Wave Energy Conversion


Matthew Johnson
*Dept. of Elec. and Comp. Engr.*
*Texas A&M University*
College Station, Texas 77843
mjohnson11@tamu.edu

Matthew C. Gardner
*Dept. of Elec. and Comp. Engr.*
*Texas A&M University*
College Station, Texas 77843
gardner1100@tamu.edu

Hamid A. Toliyat
*Dept. of Elec. and Comp. Engr.*
*Texas A&M University*
College Station, Texas 77843
toliyat@tamu.edu

Steven Englebretson
*US Corporate Research*
*ABB Inc.*
Raleigh, NC 27606
steven.englebretson@us.abb.com

Wen Ouyang
*US Corporate Research*
*ABB Inc.*
Raleigh, NC 27606
wen.ouyang@us.abb.com

Colin Tschida
*US Corporate Research*
*ABB Inc.*
Raleigh, NC 27606
colin.tschida@us.abb.com



***Abstract*—A magnetically geared machine (MGM) integrates a magnetic gear with a low torque, high speed electric machine to create a single compact high torque, low speed device with the size advantages of a mechanically geared system and the reliability of a direct drive machine. This work investigates the use of MGMs for wave energy conversion through the development of a large scale magnetically decoupled inner stator radial flux magnetically geared generator rated for 10 kW at an input speed of 30 rpm. Critical design trends are illustrated using parametric 2D and 3D finite element simulation results. Information is also provided about the prototype's mechanical structure and key magneto-mechanical design considerations, including the impact of modulator bridges and the extent of axially escaping leakage flux. The prototype's experimental stall torque of 3870 N·m represents a 99.1% match with the simulated stall torque and corresponds to volumetric and gravimetric torque densities of 82.8 kN·m/m$^3$ and 14.5 N·m/kg, respectively. Additionally, the prototype achieves an experimental efficiency of approximately 90% for operation near rated torque.**



***Keywords—cost, direct drive, efficiency, end-effects, finite element analysis, generator, large scale, magnetic gear, magnetically geared machine, optimization, radial flux, torque density, wave energy***


## I. Introduction

Wave energy is a largely untapped form of renewable energy with some promising attributes, including higher energy density, more consistency, and greater predictability than wind and solar energy [1], [2]. However, although the world's exploitable wave energy resources are on the order of 8000-80,000 TWh/year, harvesting wave energy presents significant challenges, most notably the fact that it naturally exists in the form of extremely low speed, high force or torque motion [3]. Thus, a wide array of wave energy converter technologies have been proposed [1]–[4]. The Oscillating Wave Surge Converter (OWSC) is one example of these technologies, which harnesses waves to rotate an anchored paddle back and forth in order to drive electricity generation.

While a direct-drive generator is desirable for this application because of its high reliability, the requisite machine must be very large to harness the tremendous torque necessary to generate significant electrical power from such low speed motion. Also, the extreme variation between the peak and average wave powers requires the generator to be sized for a power significantly greater than the average power that it will produce [1]. Magnetic gears are one recently proposed, promising alternative which could help address some of these issues [5]–[8]. Similarly to mechanical gears, magnetic gears can couple a high torque, low speed prime mover to a lower torque, higher speed generator. The use of a gear significantly decreases the size and cost of the required generator, which can result in a much smaller, less expensive system. Also, because magnetic gears transfer torque through the interaction of magnetic fields rather than mechanical contact, they offer a plethora of potential advantages over mechanical gears, such as reduced maintenance requirements, improved reliability, and inherent overload protection. For wave energy conversion, the inherent overload protection is especially beneficial. First, the magnetic gear will not be damaged when exposed to overload torques. Second, the magnetic gear cannot transfer more torque than its stall torque, which protects the components connected to its high speed output. Thus, the gear and generator potentially do not need to be designed to accommodate the peak wave power; instead, they can be much smaller and less expensive without sacrificing the ability to capture most of the total wave energy.

Most recent work on magnetic gears focuses on the coaxial radial flux topology [9]-[12], which consists of three concentric rotors: the high speed permanent magnet rotor (HSR), the low speed permanent magnetic rotor (LSR), and the intermediate


This research was supported by the US Department of Energy under Award Number DE-EE0006400.

ferromagnetic modulator rotor. The relationship between the number of permanent magnet (PM) pole pairs and the number of modulators is given by (1), where $P_{HS}$ is the number of HSR pole pairs, $P_{LS}$ is the number of LSR pole pairs, and $Q_M$ is the number of modulators. If the modulators are fixed, the gear ratio in (2) describes the relationship between the steady state speeds of the HSR ($\omega_{HS}$) and the LSR ($\omega_{LS}$). Alternatively, if the LSR is fixed and the modulators are allowed to rotate instead, then the gear ratio becomes positive and its magnitude increases by one. In this study, the LSR serves as the high torque rotor and the modulators are held stationary.

$$Q_M = P_{HS} + P_{LS} \tag{1}$$

$$\text{Gear Ratio} = \frac{\omega_{HS}}{\omega_{LS}} = \frac{-P_{LS}}{P_{HS}} \tag{2}$$

A magnetically geared machine (MGM) directly combines a magnetic gear with a low torque, high speed electric machine to create a single compact device with the size advantages of a mechanically geared system and the reliability of a direct drive machine. Several different MGM topologies have been proposed [13]-[17], but the inner stator radial flux MGM (IS-RFMGM) [14], [15], shown in Fig. 1, and the outer stator radial flux MGM (OS-RFMGM) [13] have received the most attention to this point and appear to be the two most promising radial flux configurations. One design study comparison of the IS-RFMGM and the OS-RFMGM found that the IS-RFMGM is capable of achieving a higher torque density [18], which is consistent with a general comparison of the results reported throughout the literature. The IS-RFMGM topology can be further sub-divided based on whether or not the magnetic gear and the integrated machine are magnetically coupled. Magnetically coupled IS-RFMGMs allow for the use of thinner (or essentially non-existent [19]) HSR back-irons between the integrated machine and gear HSR magnets, but they require the use of the same pole counts for the machine and the gear HSR. Alternatively, magnetically decoupled IS-RFMGMs require thicker HSR back-irons to decouple the fluxes of the integrated machine and the gear but allow for independent optimization of the machine and gear HSR pole counts.

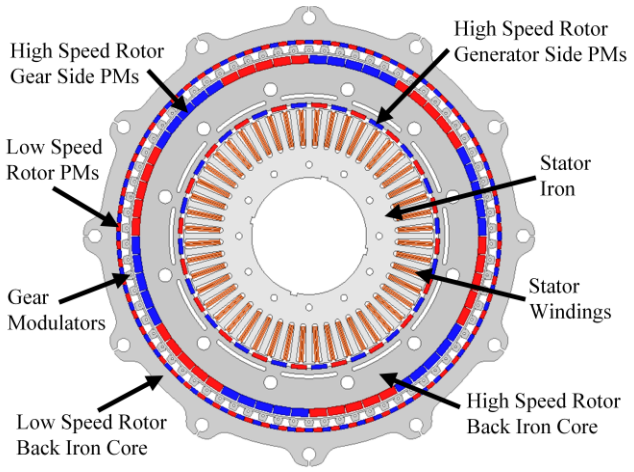


Fig. 1. Cross-sectional view of the IS-RFMGM prototype.

The vast majority of the existing literature on magnetic gear and MGM prototypes focuses on relatively small scale designs with stall torques of less than 150 N·m, and there are only a few known descriptions of prototypes with stall torques of 1000 N·m or more in the existing literature at the time of this study's publication [20], [21]. A primary objective of this work is to experimentally demonstrate the technology's feasibility at a much larger scale. In particular, this work describes the design, fabrication, and evaluation of a prototype magnetically decoupled IS-RFMGM for wave energy conversion with an OWSC. Although the prototype is scaled down relative to the tremendous torque requirements for a full scale OWSC averaging 40 kW at 1.7 rpm, its experimental stall torque of 3870 N·m is believed to be the largest ever achieved for any IS-RFMGM prototype described in the existing literature at the time of this study's publication. Much of this study is presented in [22], but this version provides additional information on the prototype's torque ripple characteristics.

## II. Design Study Methodology

In an IS-RFMGM, the designs of the magnetic gear and the integrated machine are heavily interdependent. First, the gear ratio relates the torque and speed of the integrated machine to those of the prime mover; therefore, the integrated machine should be rated for the same operating torque as the magnetic gear HSR. Second, because the machine is placed in the gear's bore, the outer radius of the machine is tied to the inner radius of the gear. Finally, to maximize torque density, the stack length of the integrated machine should be almost equal to the stack length of the gear, but slightly shorter to accommodate the additional space consumed by the end-windings.

Because the magnetic gear was assumed to be magnetically decoupled from the integrated machine, the two subsystems were simulated separately. This assumption was later verified for the final design. In order to design this prototype, the 102,060 magnetic gear parametric design variations summarized in Table I were each simulated and the results are used to illustrate important design trends and tradeoffs. Because the primary objective of the study was to demonstrate the large scale viability of MGMs, several conservative design choices were made to simplify the construction of the prototype, and further optimization could be performed to develop a more aggressive design with a higher torque density. Due to the strong interdependencies between design parameters, some derived variables were used, as suggested in [23]. In order to use the magnet material most effectively, the radial thickness of the LSR magnets, $T_{LSPM}$, is determined by the radial thickness of the HSR magnets, $T_{HSPM}$, and a derived parameter, $k_{PM}$, as shown in (3), with $k_{PM}$ not exceeding 1 [23]. A second derived parameter, $G_r$, represents the approximate gear ratio and is used to relate the number of pole pairs on the HSR and LSR according to (4). This symmetrically eliminates net radial forces on the rotors and reduces the gear's torque ripple [23], [24]. A third derived parameter, $k_{Mods}$, relates the angular fill factor of the modulators at their outer edges, $\alpha_{Mods,Out}$, to the angular fill factor of the modulators at their inner edges, $\alpha_{Mods,In}$, according to (5). As shown in Fig. 2, the

modulator poles are trapezoidal wedge shaped structures and, because there are more poles on the outer rotor than on the inner rotor, using a smaller angular fill factor on the radially outer edges of the modulators can reduce leakage flux.

$$T_{LSPM} = T_{HSPM} \cdot k_{PM} \tag{3}$$

$$P_{LS} = \begin{cases} G_r \cdot P_{HS} + 1 & \text{for } (G_r + 1) \cdot P_{HS} \text{ odd} \\ G_r \cdot P_{HS} + 2 & \text{for } (G_r + 1) \cdot P_{HS} \text{ even} \end{cases} \tag{4}$$

$$\alpha_{Mods,Out} = \alpha_{Mods,In} \cdot k_{Mods} \tag{5}$$

The construction and support of the modulator poles is one of the most challenging mechanical design features of a magnetic gear. As illustrated in Fig. 2 and specified in Table I, all designs evaluated in this parametric sweep included a 3 mm thick bridge connecting adjacent modulators on the inner edge of the modulator annulus. This strengthens the entire modulator structure and is similar to several previous magnetic gear studies [12], [15], [19], [25], [26]. Further discussion of the bridge's impact on the magnetic gear's electromagnetic performance is included with the simulation results.

Each design specified in Table I was evaluated using static 2D finite element analysis (FEA) at its stall torque position. Table II shows the key properties of the MGM active materials. The magnetic gear stack length necessary to achieve an LSR stall torque of 4200 N·m was determined for each design based on the simulated torque. Additionally, for each design, the size of the required integrated machine was determined from the machine's design curves based on the gear ratio and the magnetic gear's inner radius (the integrated machine's outer radius). This information was then used to calculate the overall volume and mass of the MGM and its constituent active materials for each parametric design case. Throughout the design process, three key metrics (in addition to efficiency) were employed to evaluate the quality of each design variation: volumetric torque density (VTD), gravimetric torque density (GTD), and active material cost (AMC). VTD is the LSR stall torque divided by the volume enclosed by the active materials (including the bore), as indicated in (6). Using the maximum of the gear axial stack length ($L_{Gear}$) and the integrated machine axial stack length ($L_{Machine}$) for the active volume calculation in the denominator of (6) inherently drives the two stack lengths to match in order to maximize VTD. GTD is simply the LSR stall torque divided by the total mass of the active materials. AMC is calculated according to (7), based on the simplifying assumption that the material price rates are fixed at the values listed in Table II [23]. In this study, VTD, GTD, and AMC do not account for magnetically inactive structural materials.

$$VTD = \frac{\text{LSR Stall Torque}}{\pi \cdot R_{Out}^2 \cdot \max\left(L_{Gear}, L_{Machine}\right)} \tag{6}$$

$$\begin{aligned} AMC = {} & (\text{PM Mass}) \cdot (\text{PM Rate}) + (\text{Steel Mass}) \cdot (\text{Steel Rate}) \\ & + (\text{Copper Mass}) \cdot (\text{Copper Rate}) \end{aligned} \tag{7}$$

TABLE I. MAGNETIC GEAR PARAMETRIC DESIGN STUDY RANGES

| Name | Description | Values | Units |
|---|---|---|---|
| $G_r$ | Nearest integer gear ratio | 7, 11, 15 | |
| $P_{HS}$ | HSR pole pairs | | |
| | For $G_r = 7$ | 3, 4, 5, … 10 | |
| | For $G_r = 11$ | 3, 4, 5, … 8 | |
| | For $G_r = 15$ | 3, 4, 5, 6 | |
| $R_{Out}$ | Gear's active outer radius | 300, 400 | mm |
| $T_{HSBI}$ | HSR back iron thickness | 10, 30, 50 | mm |
| $T_{HSPM}$ | HSR magnet thickness | 10, 12.5, … 20 | mm |
| $T_{AG}$ | Air gap thickness | 3 | mm |
| $T_{Mods}$ | Modulator thickness | 10, 15, 20 | mm |
| $T_{Bridge}$ | Modulator bridge thickness | 3 | mm |
| $k_{PM}$ | LSR magnet thickness ratio | 0.5, 0.75, 1 | |
| $T_{LSBI}$ | LSR back iron thickness | | |
| | For $T_{HSBI} = 10$ mm | 10 | mm |
| | For $T_{HSBI} = 30$ mm, 50 mm | 10, 20, 30 | mm |
| $\alpha_{Mods,In}$ | Modulator inner angular fill factor | 0.5, 0.625, 0.75 | |
| $k_{Mods}$ | Modulator angular fill factor ratio | 0.6, 0.8, 1 | |

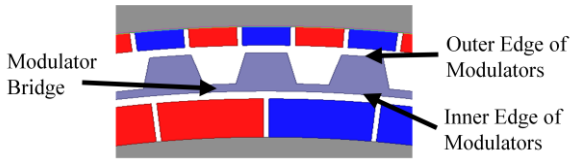


Fig. 2. Modulators with inner bridge.

TABLE II. CHARACTERISTICS OF MGM ACTIVE MATERIALS

| Material | Density | $B_r$ | Cost Rate |
|---|---|---|---|
| N42 NdFeB | 7400 kg/m$^3$ | 1.3 T | \$50/kg |
| M19 Steel (29 Gauge) | 7870 kg/m$^3$ | N/A | \$2/kg |
| Copper | 8933 kg/m$^3$ | N/A | \$10/kg |

Based on the static 2D FEA simulation results, static 3D FEA simulations were performed to evaluate the impact of end-effects on the gear designs with the best system-level performances. These 3D simulations were conducted with each design scaled to the height predicted by the corresponding 2D simulation result. Based on these 3D simulation results, the stack lengths were linearly rescaled to match the target torque. Finally, 2D transient simulations were performed for the best gear designs to determine their electromagnetic losses at full load at the nominal rated LSR speed of 30 rpm. These cross-sectional losses were linearly scaled by the requisite stack lengths predicted by the 3D simulations and used to compute the ideal electromagnetic efficiency of each gear design.

## III. DESIGN TRENDS

The graphs in Figs. 3-6 illustrate several critical MGM design trends using the results of the parametric simulation study defined in Table I. Fig. 3(a) displays the active material costs, volumetric torque densities, and gravimetric torque densities of the evaluated MGM designs based on the 2D FEA results, while Fig. 3(b) shows the same metrics for the highest performing designs based on 3D FEA results. Both graphs

show a significant tradeoff between VTD and AMC, with the maximum VTD design achieving a VTD 34.9% higher than that of the minimum AMC design but requiring a 67.6% higher AMC, based on the 3D FEA results. Fig. 4(a) illustrates the Pareto optimal front of the results in Fig. 3(b) and demonstrates that magnet thicknesses play a large role in the tradeoff between VTD and AMC. Thicker magnets tend to yield higher VTDs at the expense of elevated AMCs. Increasing the magnet thickness offers diminishing returns in VTD, because it increases the effective air gap and, thereby, the reluctance of the primary radial flux path, not just the MMF of that path. Additionally, designs with thicker magnets generally require shorter stack lengths for a fixed outer radius, which leads to more substantial 3D-effects. Furthermore, as indicated by the optimal fronts for the different HSR magnet thicknesses in Fig. 4(b), the designs with thinner magnets can also achieve slightly higher efficiencies than those with thicker magnets. This is largely due to the eddy currents in the magnets. Fig. 3(b) also depicts the performance reducing impact of 3D-effects on the design set. In particular, the maximum VTD designs typically suffer the most from 3D-effects because, for a given radius, they have the shortest stacks [23], [26], [27]. Additionally, if the gear is already longer than the generator, extending its length to compensate for 3D-effects directly impacts the entire system VTD based on (6); however, it only affects the AMC and mass of the gear and not those of the generator, so it has less impact on the AMC and GTD of the whole MGM system. Within this design set, when 3D-effects are considered, the maximum achievable VTD falls 21.9% from 135.4 kN·m/m$^3$ to 105.8 kN·m/m$^3$. In contrast, the minimum achievable AMC rises only 10.7% from \$1598 to \$1769, while the maximum GTD falls only 13.3% from 28.7 N·m/kg to 24.9 N·m/kg.

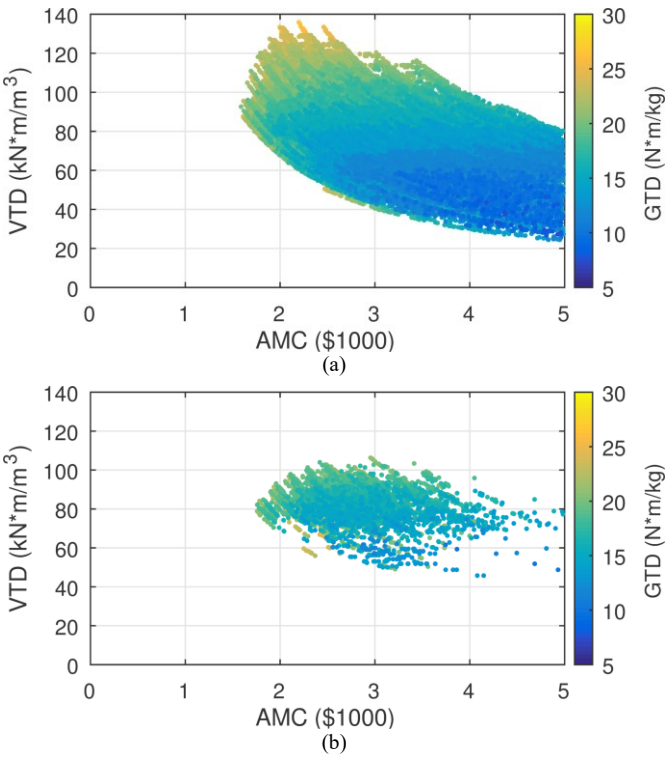


Fig. 3. MGM active material cost, volumetric torque density, and gravimetric torque density values based on (a) 2D and (b) 3D FEA simulations.

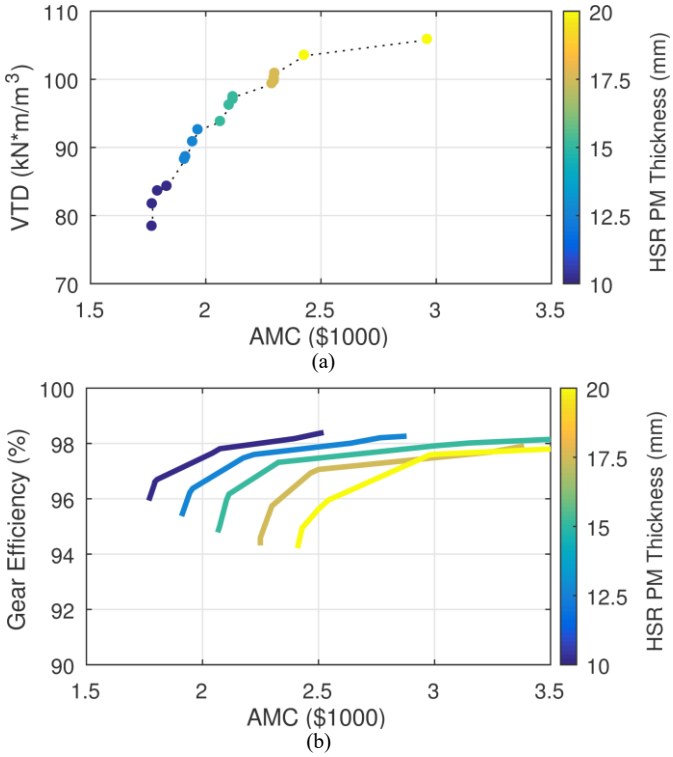


Fig. 4. Role of HSR magnet thickness in the variation of the maximum (a) MGM volumetric torque density and (b) gear electromagnetic efficiency with active material cost based on 3D FEA.

Fig. 5(a) depicts the variation of the gear's maximum achievable VTD with gear ratio and magnet thickness, while Fig. 5(b) illustrates the variation of the full MGM system's maximum achievable VTD with gear ratio and magnet thickness. It is clear that, within the range considered, thicker magnets and a lower gear ratio allow the gear to achieve a higher VTD; however, the design trends for the full MGM system are more complex. For a fixed outer radius, increasing the gear magnet thickness decreases the gear inner radius (which is the integrated generator's outer radius), especially if the back irons must be thickened to accommodate the increased flux, and this increases the required integrated generator stack

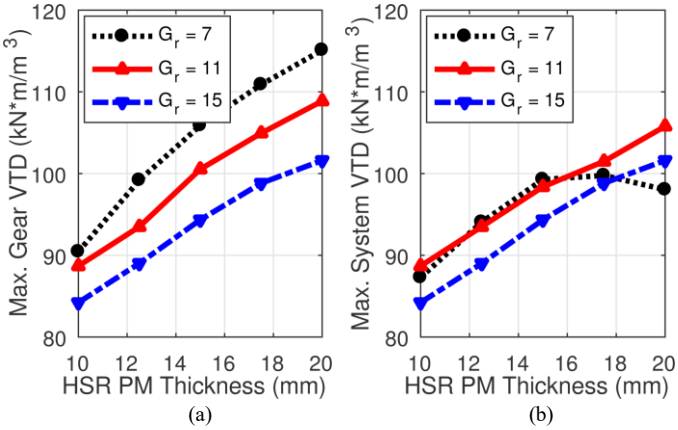


Fig. 5. Variation of maximum (a) gear and (b) system volumetric torque density with HSR magnet thickness for different gear ratios based on 3D FEA.

length. For higher gear ratios, the generator is relatively small compared to the gear and the gear stack length dictates the system stack length; therefore, increasing the magnet thickness decreases the gear and MGM system stack length, which leads to higher MGM system VTDs. However, for lower gear ratios, the generator volume is bigger and the gear volume is smaller, so the generator stack length is generally comparable to the gear stack length. For these low gear ratio designs, increasing the gear magnet thickness in the lower end of the considered range does help decrease the gear and system stack length (and thus increase the system VTD); however, beyond a certain point, the integrated generator stack length becomes dominant and increasing the gear magnet thickness further actually increases the generator stack length as previously described, which leads to a decrease in the system VTD as defined in (6).

Fig. 6 shows additional MGM system design tradeoffs involved in the selection of the gear ratio. Fig. 6(a) illustrates the mass breakdowns of the designs achieving the minimum MGM active mass for each gear ratio. Similarly, Fig. 6(b) depicts the AMC breakdowns of the designs achieving the minimum MGM AMC for each gear ratio. Increasing the gear ratio decreases the generator's active mass and AMC, but it increases the gear's active mass and AMC. For the evaluated design space, the generator active mass and AMC reductions achieved by increasing the gear ratio from 7 to 11 outweigh the corresponding gear active mass and AMC increases to yield net MGM system improvements. However, the generator active mass and AMC reductions attained by further increasing the gear ratio from 11 to 15 are essentially counterbalanced by the associated gear active mass and AMC increases, so the net system improvements are negligible. For this design scenario, increasing the gear ratio to even higher values would increase the total active mass and AMC. In general, the system-level optimum design for any MGM is achieved in part by selecting the gear ratio that strikes the appropriate balance between these two sub-systems. Based on the tradeoffs illustrated in Figs. 5 and 6 and practical design considerations, a gear ratio of approximately 11 was selected for the prototype design.

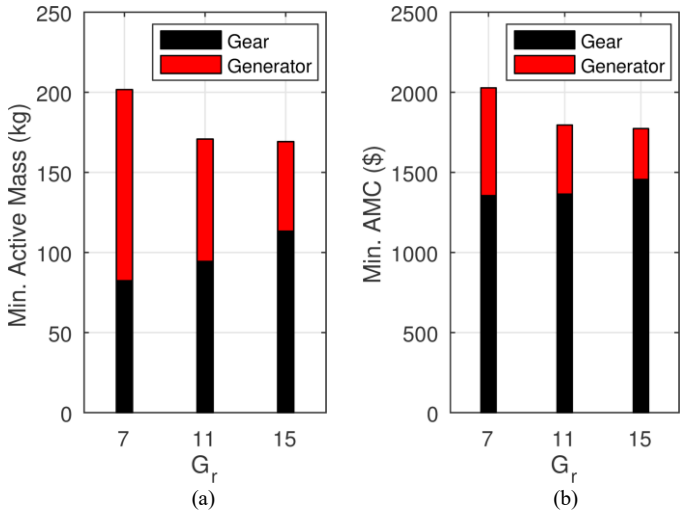


Fig. 6. Variation of minimum MGM system active (a) mass and (b) material cost with gear ratio based on 3D FEA.

## IV. Final Prototype Design

A prototype design was selected based on the parametric design study results. However, several parameters were adjusted to simplify fabrication of the prototype. Table III summarizes the final prototype design details and Fig. 1 provides a cross-sectional view of the final design. The most significant changes were made to the modulators. The modulator shape was modified to include notches at the base to retain potting between each tooth. Additionally, the modulator laminations were bonded together, and a 4.8 mm diameter hole was added in each tooth to allow the insertion of G11 glass reinforced epoxy laminate pins for alignment during assembly and to increase shear capability. Another notable change from the parametric design study was the use of rectangular magnets instead of ideal arc-shaped magnets. Collectively, these changes reduced the final 3D FEA simulated LSR stall torque from 4200 N·m to 3905 N·m.

Fig. 7 shows a cutaway view of the prototype RFMGM design. The LSR, modulators, and HSR are each supported by steel end bells, which are in turn supported by the central

TABLE III. Prototype RFMGM Final Design Specifications

| Parameter | Value* | Parameter | Value* |
|---|---|---|---|
| LSR PM Pieces/Pole | 1 | Modulators Outer Angular Fill | 0.43 |
| LSR Pole Pairs | 68 | Modulators Inner Angular Fill | 0.71 |
| Number of Modulators | 74 | Gear HSR PM Width* | 32.3 |
| Gear HSR PM Pieces/Pole | 5 | Gear Stack Length* | 93 |
| Gear HSR Pole Pairs | 6 | Generator Pole Pairs | 20 |
| Gear Ratio | 11.33:1 | Stator Slots | 48 |
| Outer Radius* | 400 | Stator Winding Turns/Coil | 45 |
| LSR Back Iron Thickness* | 31.6 | Generator Phases | 6 |
| LSR PM Thickness* | 7.5 | Stator Winding Connection | YY |
| Gear Air Gap Thicknesses* | 3 | Generator PM Thickness* | 7.6 |
| Modulators Thickness* | 15 | Generator PM Width* | 29.3 |
| Gear HSR PM Thickness* | 15 | Generator Air Gap Thickness* | 2.5 |
| HSR Back Iron Thickness* | 74.1 | Stator Bore Radius* | 110 |
| LSR PM Width* | 15.2 | Generator Stack Length* | 53 |

*All lengths, thicknesses, widths, and radii are listed in mm.

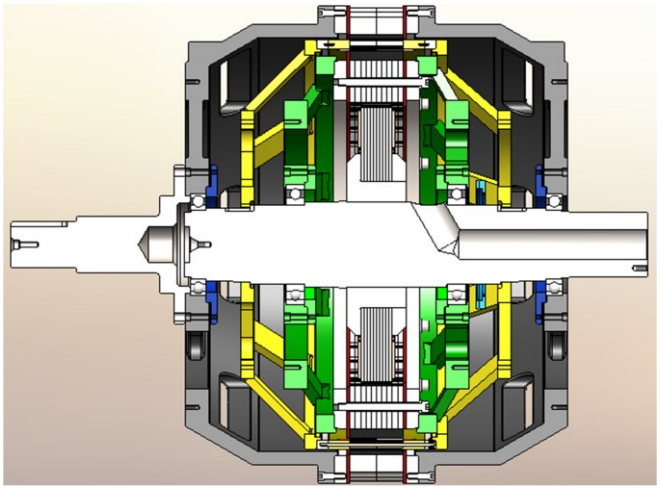

Fig. 7. Cutaway view of the RFMGM prototype

stationary shaft. A non-magnetic and non-conductive buffer of G11 glass reinforced epoxy laminate separates the magnetically active portion of the magnetic gear from each of the end bells to prevent axially escaping magnetic fields from inducing eddy current losses in the end bells. This is an important issue which has plagued multiple prior magnetic gear and MGM prototypes, resulting in significantly lower than theoretically predicted experimental efficiencies [11], [26], [29], [30]. Fig. 8(a) shows the simulated RMS magnetic flux densities axially beyond the modulators, and Fig. 8(b) shows the prototype's modulator assembly, while Fig. 9 depicts the fully assembled prototype mounted on its testbed. As indicated in Fig. 9, the prototype was driven by an induction machine connected to a mechanical gear in order to provide the necessary input torque to the MGM LSR. More details on the mechanical design of the prototype are provided in [31].

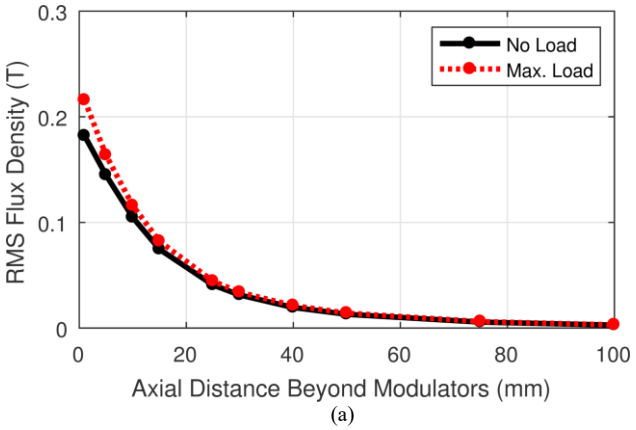


(a)

(b)

Fig. 8. (a) Simulated no load and maximum load (stall torque) leakage flux densities axially beyond the active stack in (b) the modulator assembly.

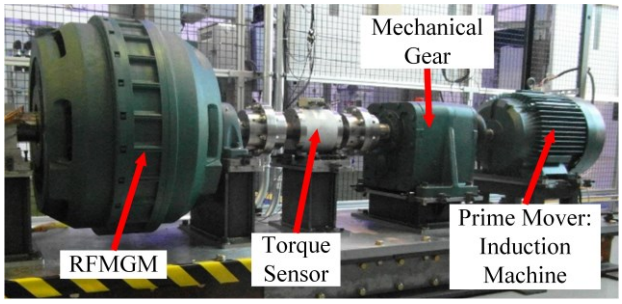


Fig. 9. RFMGM prototype mounted on testbed.

## V. Key Magneto-Mechanical Design Considerations

There are strong interrelations between the magnetic and mechanical design aspects of the magnetic gear. First, the air gap thicknesses have major ramifications both magnetically and mechanically. Increasing the air gap thickness increases the reluctance of the magnetic flux paths and decreases the torque density. Thus, besides affecting the optimum values of other design parameters such as pole count [23], [28], the stack length, outer radius, or magnet thickness must be increased to achieve the same torque. Any of these changes will impact the mechanical stresses in the gear. Mechanically, the air gaps should be much larger than fabrication tolerances and any deflections that may occur. Significant deflection can occur in the modulators because they experience large magnetic forces, which makes them challenging to secure [32]. After preliminary analysis of tolerances and modulator deflection, conservative air gaps of 3 mm were selected for the prototype.

Another major magneto-mechanical concern involves magnetic flux leaking axially beyond the magnetically active portion of the gear [27]. As previously noted, this magnetic flux can cause significant losses in conductive structural material beyond the active portion of the gear [11], [26], [29], [30]. Fig. 8(a) shows the prototype's simulated flux density axially beyond the modulators, where flux leakage is the strongest. To mitigate losses in the end bells, 36 mm axially thick non-conductive G11 standoffs were placed between the magnetically active portion of the gear and the end bells.

A third magneto-mechanical consideration is the thickness and position of the bridge between the modulators. Increasing the bridge thickness improves the modulators' mechanical strength, rigidity, and ease of handling, but it also decreases the gear's stall torque, as indicated by Fig. 10(a). The results in Fig. 10(a) are based on simulated variations of the bridge thickness and position in the final prototype design, where the bridge position (BP) indicates the radial location of the bridge, with 0 and 1 corresponding to the inner and outer edges of the modulators, respectively. Fig. 10(a) indicates that the decrease in stall torque is minimized by placing the bridge on the inner edge of the modulators and making it as thin as mechanically permissible, which is consistent with the conclusions of [12].

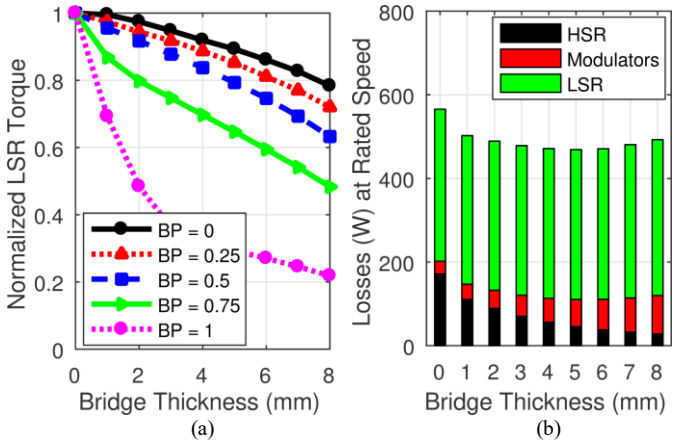


(a) (b)

Fig. 10. Simulated impact of the modulator bridge thickness in the final MGM prototype design on (a) stall torque as the bridge position (BP) is varied and on (b) electromagnetic losses in the gear.

Because the bridge provides a leakage path for the magnetic flux, increasing its thickness increases the leakage flux. Additionally, because the LSR has many more poles than the HSR, moving the bridge towards the LSR significantly increases the leakage flux and, within the range considered, the bridge's position is generally more impactful than its thickness. However, this leakage path affects higher order spatial flux harmonics more significantly than lower order harmonics. This filters out some of these unwanted harmonics, which can reduce losses [26]. Fig. 10(b) shows the simulated loss breakdown for the prototype as the bridge thickness changes with the bridge position fixed to the modulators' inner edge. As the bridge thickness increases, the losses in the HSR decrease significantly due to the filtering effect. However, the design's stack length must increase to maintain the stall torque, which increases the gear volume and eventually leads to a rise in total losses once the bridge thickness crosses a certain point. Core losses in the bridge itself also contribute to the increase in modulator losses that occurs as the bridge thickness increases.

## VI. Simulated and Experimental Results

Fig. 11 shows the simulated electromagnetic losses in the magnetic gear based on transient 2D FEA. Fig. 11(a) indicates that the gear's electromagnetic losses are nearly independent of load and almost exclusively dependent on speed, leading to higher electromagnetic efficiencies at higher loads as shown in Fig. 11(b). Fig. 11(c) depicts the different electromagnetic no load loss components. Due to the modulator bridge's harmonic filtering effect, losses in the HSR are minimal. Most of the losses occur in the LSR, especially at higher speeds where the eddy current losses in the LSR PMs are dominant.

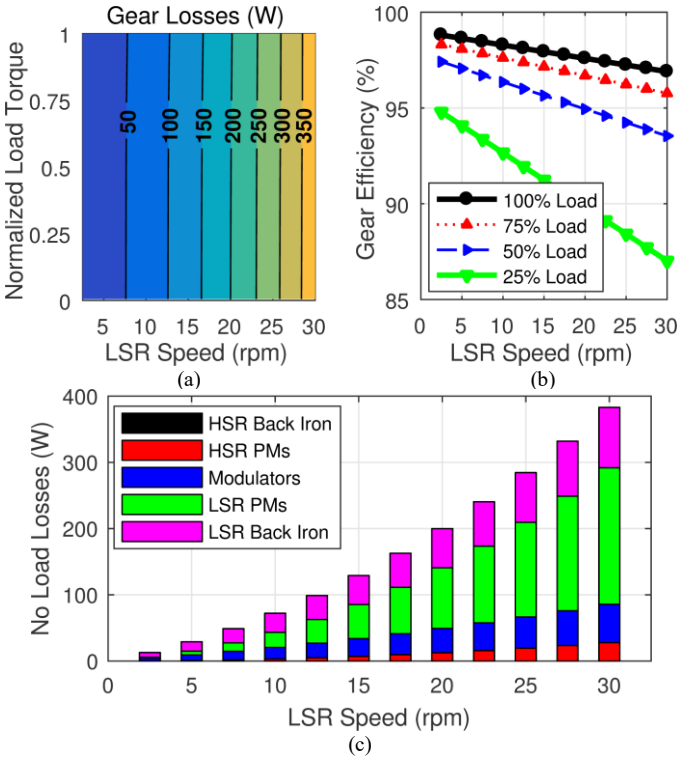


Fig. 11. Simulated magnetic gear electromagnetic (a) losses and (b) efficiency at different load torques (relative to the stall torque) and speeds and (c) no load loss component breakdown.

Figs. 12 and 13 show a comparison of the simulated and measured results for the RFMGM prototype. The LSR torque angle curve measurements in Fig. 12 were obtained by locking the HSR and using a dial indicator to measure the position of the LSR. Because the large torque on the HSR caused it to deflect slightly, even when locked, a second dial indicator was used to measure this deflection. Dial indicators were employed to achieve high accuracy even with relatively small mechanical angular displacements. The torque angle, $\theta_{Torque}$, is calculated according to (8) from the positions of both the HSR, $\theta_{HS}$, and the LSR, $\theta_{LS}$, relative to the equilibrium position. Fig. 12 shows excellent consistency between the 3D FEA simulation results and the experimental measurements. The measured LSR stall torque of 3870 N·m is a 99.1% match with the simulated stall torque of 3905 N·m. Based on the experimental stall torque, the prototype achieved a VTD of 82.8 kN·m/m$^3$ and a GTD of 14.5 N·m/kg with a nominal AMC of $2274.

$$\theta_{Torque} = P_{HS} \cdot \theta_{HS} + P_{LS} \cdot \theta_{LS} \quad (8)$$

The RFMGM prototype's steady-state performance was characterized at different fixed speeds using multiple fixed resistance YY-connected loads. Fig. 13 compares the simulated and experimental performances of the prototype under the different operating conditions. Fig. 13(a) indicates that the prototype achieves the rated 10 kW output at the rated 30 rpm LSR input speed with an 18.8 Ω resistive load on each phase. With the smaller resistances, the prototype achieves the rated torque at lower speeds. The results in Figs. 13(b) and 13(c) reveal that the prototype experienced higher experimental losses than predicted by FEA. This discrepancy is due in part to the fact that the simulated losses do not include the mechanical losses associated with the bearings and windage, which are likely larger in an MGM than in a conventional direct-drive machine due to the HSR. However, further work is required to determine the exact sources of this discrepancy. Due to the aforementioned precautions with the non-magnetic, non-conductive G11 buffers, losses in the end bells and other inactive material outside of the active MGM stack should be minimal. Despite these differences, Fig. 13(c) illustrates that the prototype still achieves an experimental efficiency of approximately 90% for operation near rated torque.

The prototype's experimental torque ripple characteristics were also recorded, and the results are summarized in Table IV and Figs. 14 and 15, along with simulated 2D FEA torque

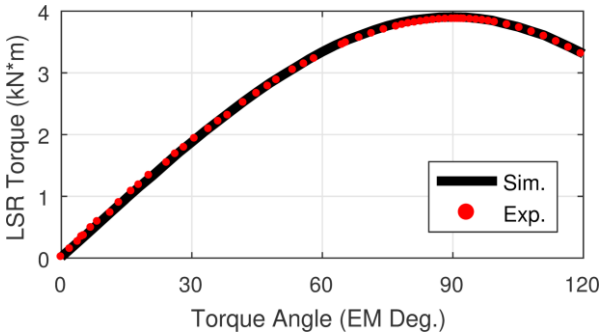


Fig. 12. Simulated and experimental MGM LSR torque angle curves.

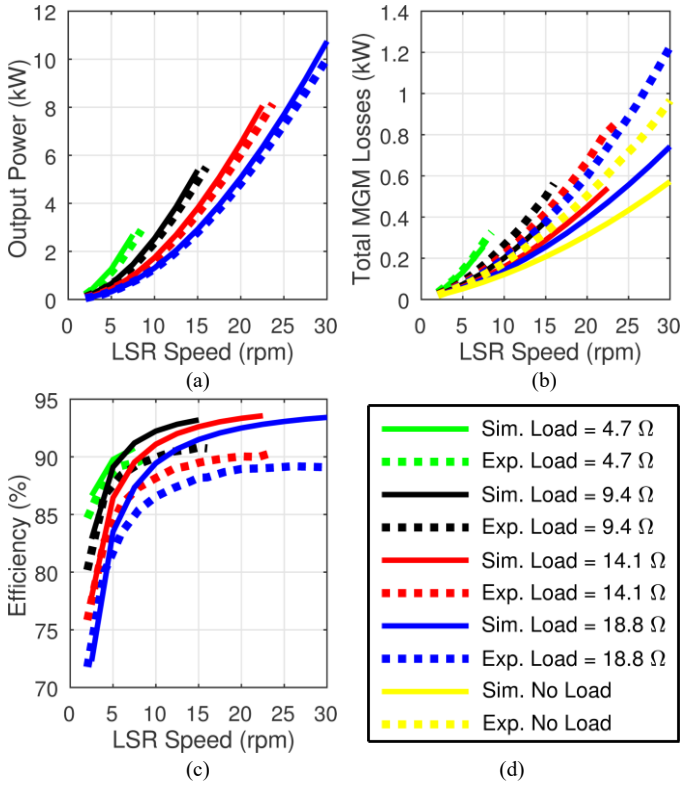


Fig. 13. Simulated and experimental MGM (a) output power, (b) total losses, and (c) efficiency at different speeds and (d) resistive loads.

design variations. These additional variations are created by changing only the LSR pole pair count (relative to the prototype design), which also changes the modulator count to satisfy (1). The prototype's experimental torque ripple, illustrated in Fig. 14, was larger than the torque ripple predicted by the 2D FEA model, likely due to a combination of measurement noise, torque variations from other components of the experimental setup, and manufacturing tolerances. Nevertheless, the LSR torque ripple was still extremely small, especially when compared to the LSR stall torque. Torque ripple characteristics are also provided for $P_{LS}$ = 66 ($Q_M$ = 72) and $P_{LS}$ = 67 ($Q_M$ = 73) variations of the prototype design in order to illustrate the value of using the HSR and LSR pole pair count relationship defined in (4), in which the LSR pole pair count is determined by the HSR pole pair count and $G_r$, which represents the integer part of the desired gear ratio. This approach keeps the LCMs between $P_{HS}$, $P_{LS}$, and $Q_M$ relatively high and avoids integer gear ratios which result in extremely high torque ripple, especially on the HSR, as demonstrated by the $P_{LS}$ = 66 design variation. This relationship also ensures that an even number of modulators is always selected, which symmetrically eliminates net radial forces on the rotors. This is demonstrated by the fact that the $P_{LS}$ = 67 design variation's modulator assembly experiences a simulated rotating net radial force of 1032 N during full load operation, while the prototype and the $P_{LS}$ = 66 design variation ideally experience no net radial forces on their modulator assemblies and rotors. Thus, the reduction of the effective bearing loads resulting from choosing an even number of modulators is worth the negligible difference in torque ripple between the $P_{LS}$ = 67 and $P_{LS}$ = 68 design variations. At lower pole counts the increase in torque

TABLE IV. MGM TORQUE RIPPLE CHARACTERISTICS

| Data Set | Data Type | Pk-Pk Torque Ripple (N·m) | | Pk-Pk Torque Ripple/(Stall Torque) | |
|---|---|---|---|---|---|
| | | HSR | LSR | HSR | LSR |
| Prototype ($P_{LS}$ = 68) | Experimental | N/A | 44.4 | N/A | 1.15% |
| Prototype ($P_{LS}$ = 68) | 2D FEA | 9.2 | 0.7 | 2.2% | 0.02% |
| $P_{LS}$ = 66 Variation | 2D FEA | 578.3 | 88.7 | 134.5% | 1.88% |
| $P_{LS}$ = 67 Variation | 2D FEA | 9.2 | 0.7 | 2.2% | 0.02% |

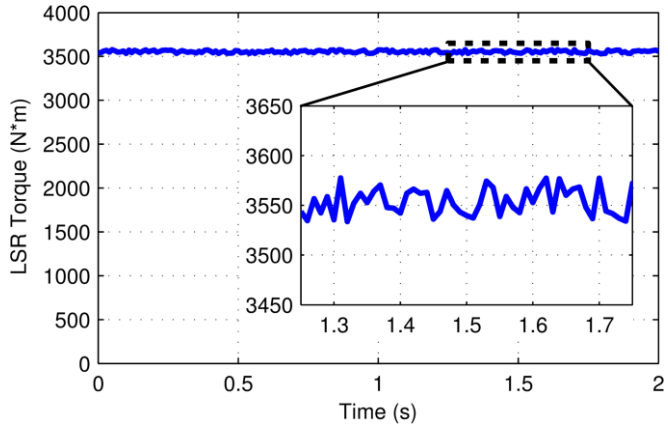


Fig. 14. Experimental torque ripple data at an LSR speed of 30 rpm.

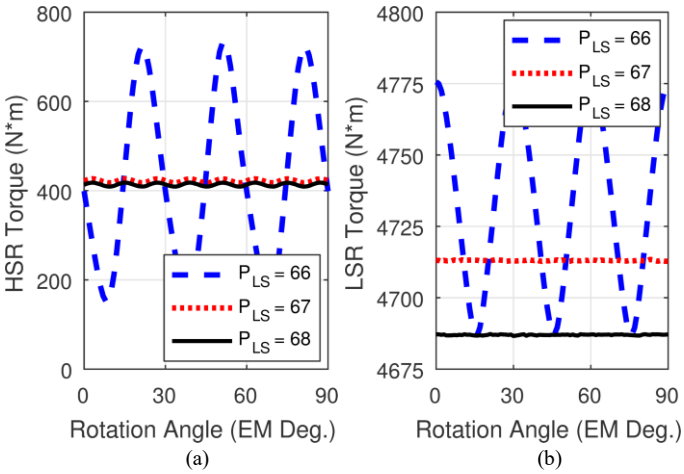


Fig. 15. Simulated (a) HSR and (b) LSR torque ripple characteristics for the MGM prototype and LSR pole count design variations based on 2D FEA.

ripple associated with always using an even modulator pole count may become more pronounced; however, in most cases, the benefits of eliminating the unbalanced net radial forces still more than compensate for this increase in torque ripple.

## VII. CONCLUSION

Waves offer a relatively untapped, bountiful source of renewable energy, but this energy must be harvested from very low speed, high force or torque motion, which is also characterized by high peak-to-average "overload" forces or torques. This study investigates the use of magnetically geared machines as a potential solution to harness this energy; it describes the design, construction, analysis, and experimental evaluation of a large scale magnetically-decoupled inner stator radial flux magnetically geared machine prototype. The

prototype achieved a stall torque of 3870 N·m, which is believed to be the largest of any IS-RFMGM prototype described in the existing literature at the time of this study's publication. This experimental stall torque is a 99.1% match with the simulated 3D FEA stall torque and corresponds to a volumetric torque density of 82.8 kN·m/m$^3$ and a gravimetric torque density of 14.5 N·m/kg with a nominal active material cost of $2274. Furthermore, the prototype was approximately 90% efficient when operating in steady-state near its rated torque and exhibited minimal torque ripple. Thus, the technology has tremendous potential for high torque, low speed applications, such as wave and wind energy harvesting, traction, and oil and gas production.

In addition, this study's simulation results support several interesting conclusions. First, selection of the optimal gear ratio requires simultaneous evaluation of the magnetic gear and the generator because, as the gear ratio increases, the volume, cost, and mass increase for the gear but decrease for the generator. For this study, a gear ratio of 11.33 was selected. Second, there is a significant difference between minimal AMC designs and maximal VTD designs. Third, end-effects can significantly reduce performance. In this study, end-effects degraded the optimal achievable VTD by 21.9%, AMC by 10.7%, and GTD by 13.3%. Fourth, the gear's electromagnetic losses are nearly independent of the load torque, so it is most efficient at full load. Finally, the modulator bridge's harmonic filtering effect keeps the losses in the HSR relatively small, and most of the gear's losses are concentrated in the LSR.

Nonetheless, significant future work is required to develop the technology and realize its commercial potential. For wave energy conversion, future studies should investigate MGMs' performances with oscillating input motion sources analogous to that provided by an actual OWSC, including transient overload torques, and the development of maximum wave energy extraction algorithms using an active converter load. Preliminary analysis of some of these topics is provided in [33] using the prototype described in this work. For all applications, further research is necessary to evaluate the impact of magnetic design decisions on tradeoffs between magnetic material requirements, inactive structural material requirements, and manufacturability. Regardless, this study provides a tangible demonstration of MGMs' tremendous promise for use in large scale, high torque applications.

## ACKNOWLEDGMENT

The authors would like to thank ANSYS for their generous support of the EMPE lab through the provision of FEA software. The authors would also like to thank Andy Meyer, Dave McKinney, Mike Brinkmann, and Paul Humphries for their significant contributions to the engineering and assembly and the staff at ABB/Baldor's Gainesville motor plant for their support of the prototype construction.

This material is based upon work supported by the Department of Energy under Award Number DE-EE0006400. This report was prepared as an account of work sponsored by an agency of the United States Government. Neither the United States Government nor any agency thereof, nor any of their employees, makes any warranty, express or implied, or assumes any legal liability or responsibility for the accuracy, completeness, or usefulness of any information, apparatus, product, or process disclosed, or represents that its use would not infringe privately owned rights. Reference herein to any specific commercial product, process, or service by trade name, trademark, manufacturer, or otherwise does not necessarily constitute or imply its endorsement, recommendation, or favoring by the United States Government or any agency thereof. The views and opinions of authors expressed herein do not necessarily state or reflect those of the United States Government or any agency thereof.

## REFERENCES

[1] B. Czech and P. Bauer, "Wave Energy Converter Concepts: Design Challenges and Classification," *IEEE Ind. Electron. Mag.*, vol. 6, no. 2, pp. 4-16, June 2012.

[2] T. Brekken, "Fundamentals of ocean wave energy conversion, modeling, and control," in *Proc. IEEE Int. Symp. Ind. Electron.*, 2010, pp. 3921-3966.

[3] A. Muetze and J. G. Vining, "Ocean Wave Energy Conversion - A Survey," in *Conf. Rec. IEEE Ind. Appl. Soc. Annu. Meeting*, 2006, pp. 1410-1417.

[4] M. A. Mueller, H. Polinder, and N. Baker, "Current and Novel Electrical Generator Technology for Wave Energy Converters," in *Proc. IEEE Int. Elect. Mach. and Drives Conf.*, 2007, pp. 1401–1406.

[5] S. Pakdelian and H. A. Toliyat, "Trans-Rotary Magnetic Gear for Wave Energy applicaion," in *Proc. IEEE Power and Energy Soc. General Meeting*, 2012 , pp. 1-4.

[6] S. Hazra, S. Bhattacharya, K. K. Uppalapati, and J. Bird, "Ocean energy power take-off using oscillating paddle," in *Proc. IEEE Energy Convers. Congr. and Expo.*, 2012, pp. 407-413.

[7] K. K. Uppalapati, J. Z. Bird, D. Jia, J. Garner, and A. Zhou, "Performance of a magnetic gear using ferrite magnets for low speed ocean power generation," in *Proc. IEEE Energy Convers. Congr. and Expo.*, 2012, pp. 3348-3355.

[8] W. Li, K. T. Chau, and J. Z. Jiang, " Application of Linear Magnetic Gears for Pseudo-Direct-Drive Oceanic Wave Energy Harvesting," *IEEE Trans. Magn.*, vol. 47, no. 10, pp. 2624-2627, Oct. 2011.

[9] K. Atallah and D. Howe, "A novel high-performance magnetic gear," *IEEE Trans. Magn.*, vol. 37, no. 4, pp. 2844–2846, Jul. 2001.

[10] K. Atallah, S. D. Calverley, and D. Howe, "Design, analysis and realisation of a high-performance magnetic gear," *IEE Proc. Elec. Power Appl.*, vol. 151, no.2, pp. 135–143, Mar. 2004.

[11] P. O. Rasmussen, T. O. Anderson, F. T. Jorgensen, and O. Nielsen, "Development of a high-performance magnetic gear," *IEEE Trans. Ind. Appl.*, vol. 41, no. 3, pp. 764-770, May-June 2005.

[12] N. W. Frank and H. A. Toliyat, "Analysis of the Concentric Planetary Magnetic Gear With Strengthened Stator and Interior Permanent Magnet Inner Rotor," *IEEE Trans. Ind. Appl.*, vol.47, no.4, pp.1652-1660, July-Aug. 2011.

[13] K. Atallah, J. Rens, S. Mezani, and D. Howe, "A Novel "Pseudo" Direct-Drive Brushless Permanent Magnet Machine," *IEEE Trans. Magn.*, vol. 44, no. 11, pp. 4349-4352, Nov. 2008.

[14] L. Jian, K. T. Chau, and J. Z. Jiang, "A Magnetic-Geared Outer-Rotor Permanent-Magnet Brushless Machine for Wind Power Generation," *IEEE Trans. Ind. Appl.*, vol. 45, no. 3, pp. 954–962, May–June 2009.

[15] P. O. Rasmussen, H. H. Mortensen, T. N. Matzen, T. M. Jahns, and H. A. Toliyat, "Motor integrated permanent magnet gear with a wide torque-speed range," in *Proc. IEEE Energy Convers. Congr. and Expo.*, 2009, pp. 1510-1518.

[16] R.-J. Wang, L. Brönn, S. Gerber, and P. M. Tlali, "Design and evaluation of a disc-type magnetically geared PM wind generator," in *Proc. Int. Conf. Power Eng., Energy, and Elect. Drives*, 2013, pp.1259-1264.

[17] M. Johnson, M. C. Gardner and H. A. Toliyat, "Design and Analysis of an Axial Flux Magnetically Geared Generator," *IEEE Trans. Ind. Appl.*, vol. 53, no. 1, pp. 97-105, Jan.-Feb. 2017.

[18] S. Gerber and R. J. Wang, "Torque capability comparison of two magnetically geared PM machine topologies," in *Proc. IEEE Int. Conf. Ind. Technol.*, 2013, pp. 1915-1920.

[19] S. Gerber and R. J. Wang, "Design and Evaluation of a Magnetically Geared PM Machine," *IEEE Trans. Magn.*, vol. 51, no. 8, pp. 1-10, Aug. 2015.

[20] A. Penzkofer, "Analytical Modelling and Analysis of Magnetic Gears and Pseudo Direct Drives for Large Wind Turbines," Ph.D. Thesis, Dept. Electronic and Electrical Eng., Univ. of Sheffield, Sheffield, UK, 2016.

[21] K. Davey, T. Hutson, L. McDonald, and G. Hutson, "The Design and Construction of Cycloidal Magnetic Gears," in *Proc. IEEE Int. Elect. Mach. and Drives Conf.*, 2017, pp. 1-8.

[22] M. Johnson, M. C. Gardner, H. A. Toliyat , S. Englebretson, W. Ouyang and C. Tschida, "Design, Construction, and Analysis of a Large Scale Inner Stator Radial Flux Magnetically Geared Generator for Wave Energy Conversion," in *Proc. IEEE Energy Convers. Congr. and Expo.*, 2017, pp. 5017-5024.

[23] M. Johnson, M. C. Gardner, and H. A. Toliyat, "Design Comparison of NdFeB and Ferrite Radial Flux Surface Permanent Magnet Coaxial Magnetic Gears," *IEEE Trans. Ind. Appl.*, vol. 54, no. 2, pp. 1254-1263, Mar.-Apr. 2018.

[24] N. W. Frank and H. A. Toliyat, "Gearing ratios of a magnetic gear for wind turbines," in *Proc. IEEE Int. Elect. Mach. and Drives Conf.*, 2009, pp. 1224–1230.

[25] P. M. Tlali, S. Gerber and R. J. Wang, "Optimal Design of an Outer-Stator Magnetically Geared Permanent Magnet Machine," *IEEE Trans. Magn.*, vol. 52, no. 2, pp. 1-10, Feb. 2016.

[26] S. Gerber and R. J. Wang, "Evaluation of a prototype magnetic gear," in *Proc. IEEE Int. Conf. Ind. Technol.*, 2013, pp. 319-324.

[27] S. Gerber and R-J. Wang, "Analysis of the end-effects in magnetic gears and magnetically geared machines," in *Proc. IEEE Int. Conf. Elect. Mach.*, 2014, pp. 396-402.

[28] M. C. Gardner, B. E. Jack, M. Johnson, and H. A. Toliyat, "Comparison of Coaxial Radial Flux Magnetic Gears Independently Optimized for Volume, Cost, and Mass," in *Proc. IEEE Int. Elect. Mach. and Drives Conf.*, 2017, pp. 1-8.

[29] T. V. Frandsen and P. O. Rasmussen, "Loss investigation of Motor Integrated Permanent Magnet Gear," in *Proc. Int. Conf. Elect. Mach. and Syst.*, 2014, pp. 2673-2679.

[30] T. V. Frandsen and P. O. Rasmussen, "Practical investigation of end effect losses in a Motor Integrated Permanent Magnet Gear," in *Proc. IEEE Energy Convers. Congr. and Expo.*, 2015, pp. 4425-4432.

[31] C. Tschida, W. Ouyang, and S. Englebretson, "Advanced Direct Drive Electric Machine Enabling High Torque at Low Speeds," in *Proc. ASME Power and Energy Conf.*, 2017, pp. 1-9.

[32] K. K. Uppalapati and J. Z. Bird, "An Iterative Magnetomechanical Deflection Model for a Magnetic Gear," *IEEE Trans. Magn.*, vol. 50, no. 2, pp. 245-248, Feb. 2014.

[33] S. Hazra, P. Kamat, S. Bhattacharya, W. Ouyang and S. Englebretson, "Power Conversion and Control of a Magnetic Gear Integrated Permanent Magnet Generator for Wave Energy Generation," in *Proc. IEEE Energy Convers. Congr. and Expo.*, 2017, pp. 5065-5072.